SCIENTIFIC REPORTS

OPEN

SUBJECT AREAS:
MATERIALS CHEMISTRY
INORGANIC CHEMISTRY
SOFT MATERIALS
NANOSCALE MATERIALS

Received
2 November 2012

Accepted
6 February 2013

Published
25 February 2013

Correspondence and requests for materials should be addressed to H.M.Y. (hmyang@csu.edu.cn) or S.M. (s.mann@bristol.ac.uk)

Controlled Assembly of Sb_2S_3 Nanoparticles on Silica/Polymer Nanotubes: Insights into the Nature of Hybrid Interfaces

Huaming Yang[1,2], Mei Li[2], Liangjie Fu[1], Aidong Tang[1] & Stephen Mann[2]

[1]Department of Inorganic Materials, School of Resources Processing and Bioengineering, Central South University, Changsha 410083, China, [2]Centre for Organized Matter Chemistry, School of Chemistry, University of Bristol, Bristol BS8 1TS, UK.

Silica nanotubes can serve as high aspect ratio templates for the deposition of inorganic nanoparticles to form novel hybrids. However, the nature of the interfacial binding is still an unresolved challenge when considered at the atomic level. In this work, novel nanocomposites have been successfully fabricated by the controlled nucleation and assembly of Sb_2S_3 nanoparticles on the surface of mercaptopropyl-functionalized silica/polymer hybrid nanotubes (HNTs). The Sb_2S_3 nanoparticles were strongly attached to the HNTs surface by interactions between the pendent thiol groups and inorganic sulfur atoms. Detailed analysis of the geometric and electronic structure using first–principle density functional theory demonstrates charge transfer from the nanoparticles to the underlying HNTs at the Sb_2S_3/HNTs interfaces. Formation of a packed array of Sb_2S_3 nanoparticles on the HNTs results in mixing of the electronic states of the components, and is mediated by the mercaptopropyl bridges between Sb_2S_3 and the outer layer of the HNTs.

Semiconductor nanomaterials have recently attracted considerable attention due to their novel properties and potential applications in electronic and optoelectronic devices. Among these nanomaterials, antimony trisulfide (Sb_2S_3) is recognized as a prospective material suitable for solar energy conversion, thermoelectric technologies and optoelectronic devices in the IR region[1–5]. Single-crystal Sb_2S_3 nanorods have been prepared by sonochemical methods using ionic fluids[6], or by solvothermal/hydrothermal procedures involving a variety of xanthate, dithiocarbamate, dithiophosphate and other types of single-source precursors[7,8]. However, the formation of Sb_2S_3 nanoparticles using simple chemical methods has not been extensively studied. Moreover, although changes in the crystal morphology, for example from nanorods to complex flower-like arrangements, can be induced by using surfactant-mediated hydrothermal procedures, or by regulating the type of precursor and reaction time employed in solvothermal methods[9], the fabrication of spatially patterned, multicomponent (hybrid) materials comprising Sb_2S_3 nanoparticles has not explored in detail, even though research on hybrid materials has become a key focus in advanced materials research[10–15]. In particular, as demonstrated in other systems such as the decoration of carbon or silica nanotubes with a wide variety of inorganic nanoparticles[16–20], the possibility of preparing hybrid functional nanomaterials via selectively assembling Sb_2S_3 nanoparticles on the surface of preformed nanotubular templates should provide a range of new opportunities.

In this paper, we fabricate hybrid nanostructures comprising uniformly packed arrays of Sb_2S_3 nanoparticles arranged on the silicified outer surface of highly elongated diblock copolymer nanotubes. The thiol-functionalized silica-coated polymer nanostructures are prepared by a non-equilibrium self-assembly process involving the water-induced transformation of particles of a swollen lamellar gel phase comprising poly (ethylene oxide)-b-poly (1,2-butylene oxide) ($E_{16}B_{22}$), tetraethoxysilane, and 3-mercaptopropyl triethoxysilane ($HS(CH_2)_3Si(OC_2H_5)_3$)[21]. The silicified myelin-like hybrid nanotubules (HNTs) are then incubated at room temperature in a water/ethylene glycol reaction solution containing antimony chloride ($SbCl_3$) and thioacetamide (CH_3CSNH_2) to generate high aspect ratio silica/polymer nanostructures decorated with closely packed arrangements of discrete Sb_2S_3 nanoparticles. We use a range of physical methods to investigate the structural and morphological aspects of the as-synthesized and thermally treated nanocomposites, and to elucidate the nature of the mercaptopropyl-functionalized silica surface and its interface with clusters of Sb_2S_3. Moreover, because the hybrid nanocomposites are integrated structures rather than physical mixtures, the role of the interfacial bonding

is of central importance for understanding the structure and properties of such materials[22]. We therefore use theoretical calculations of geometric structures and electronic properties based on the first-principles density functional theory (DFT) to provide a detailed atomic level model of the hybrid interface associated with the as-synthesized HNTs before and after decoration with Sb_2S_3 nanoparticles.

Results

Addition of an ethylene glycol solution of antinomy chloride to a suspension of thiol-functionalized silica/polymer ($E_{16}B_{22}$) myelin-like hybrid nanotubules (HNTs) dispersed in aqueous thioacetamide (TAA) produced a lemon-yellow colored solution of soluble $[Sb(TAA)_x]^{3+}$ complexes that decomposed through nucleophilic attack of water molecules to release S^{2-} ions. The corresponding increase in supersaturation with respect to the nucleation of Sb_2S_3 was associated with the formation of an orange dispersion after 5 min, which turned brick-red when left unstirred for 24 h at room temperature (Fig. 1a). XRD analysis of the brick-red precipitate

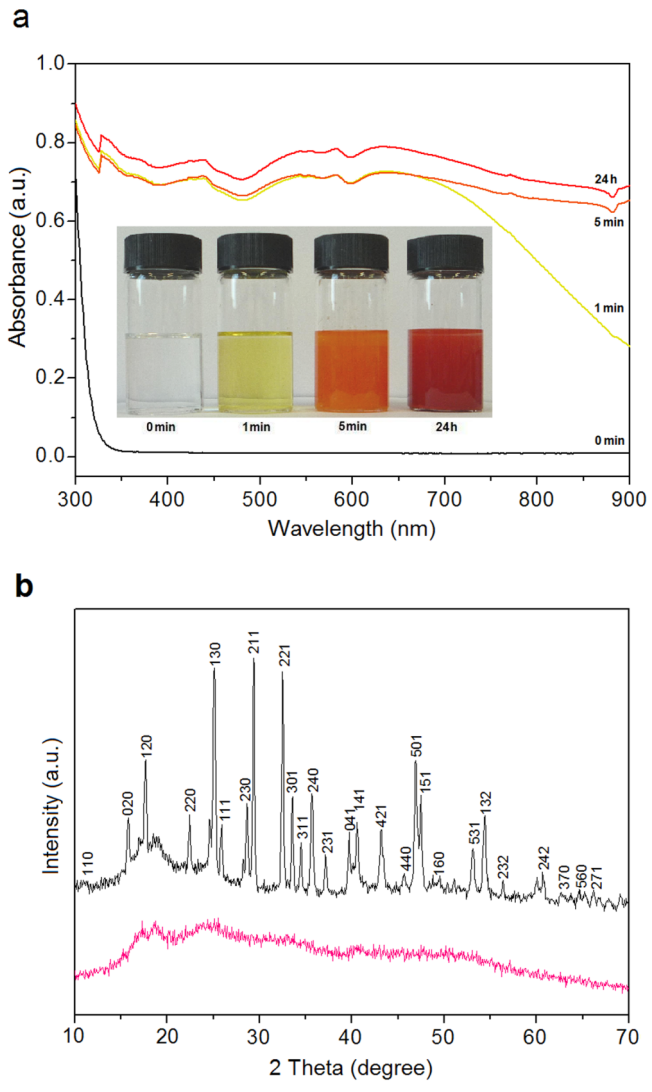

Figure 1 | Formation and phase structure of Sb_2S_3/HNTs. (a) UV-vis spectra of the reaction solution during the synthesis of Sb_2S_3/HNTs at different reaction times: t = 0 min, colorless; t = 1 min, lemon yellow; t = 5 min, orange and t = 24 h, brick red. Inset shows corresponding color changes of the reaction solution. (b) XRD patterns of as-synthesized (pink) and calcined Sb_2S_3/HNTs at 400°C under N_2 (black).

indicated that the as-synthesized Sb_2S_3/HNTs nanocomposites were amorphous, whereas subsequent calcination of the hybrid material at 400°C under N_2 resulted in a well-crystallized product exhibiting sharp reflections that were indexed to the orthorhombic Sb_2S_3 phase (a = 11.226 Å, b = 11.307 Å and c = 3.835 Å; JCPDS File 06–0474, Fig. 1b). Formation of the orthorhombic phase was consistent with other synthetic routes involving solvothermal, hydrothermal, sonochemical or pulsed growth procedures[3,6,23], and was also replicated in control experiments prepared as above but in the absence of the HNTs (Supplementary Fig. S1 and Table S1), indicating that the silicified polymer nanotubes had no effect on the crystallinity of the Sb_2S_3 produced by calcination (all the polymer component was decomposed at 350°C (TGA and DSC data not shown). The as-synthesized Sb_2S_3/silica product exhibited a broad peak around 290 cm^{-1} characteristic of amorphous materials, while the calcined product exhibited six characteristic Raman peaks at 150, 186, 249, 291, 371 and 451 cm^{-1} (Supplementary Fig. S2), in good agreement with previous Raman spectroscopy studies[2,23]. The peak around 290 cm^{-1} and relatively broad peak at 451 cm^{-1} were ascribed to the SbS_3 pyramidal unit with C_{3v} symmetric modes, and symmetric stretching of the Sb-S-S-Sb linkage, respectively.

TEM images of the as-synthesized HNTs prepared at a Sb:Si molar ratio of 1 : 1 showed a network of soft, flexible, highly elongated nanostructures, which were ca. 150 nm in diameter and a few micrometres in length (Fig. 2a). High-magnification TEM images showed the presence of discrete nanoparticles that were uniformly assembled on the external surface of the HNTs (Fig. 2b, c). EDX analysis of the Sb_2S_3/HNTs showed high intensity peaks for S and Sb, along with a negligible peak for Si (Fig. 2d), suggesting that the surface-embedded nanoparticles consisted of amorphous Sb_2S_3. Particle size measurements gave a distribution of nanoparticle dimensions across a range from 4 to 13 nm, with an average size of 7.8 nm (Fig. 2e). Significantly, thermal treatment of the Sb_2S_3/HNTs at 400°C under N_2 gave an inorganic silica/Sb_2S_3 product that exhibited partial retention of the filamentous morphology of the nanotubular template (Fig. 2f). SAED patterns displayed reflections consistent with well-crystallized Sb_2S_3 (Fig. 2g), in accordance with the XRD results obtained from the bulk sample (Fig. 1b).

We investigated the nature of the interfacial interactions through FTIR spectroscopic and XPS analysis. FTIR spectra of the native HNTs showed a strong characteristic peak at 1105 cm^{-1}, consistent with the superimposition of a C–O stretching vibration in the C–O–C structure of the polymer and Si–O stretching vibration in the silica overlayer of the HNTs (Supplementary Fig. S3). Peaks at 2871–2970 cm^{-1} and 1460 cm^{-1}, corresponding to the polymer C–H stretching and C–H scissor vibrations, respectively, were also observed[21]. A broad O–H stretching vibration peak was present at 3437 cm^{-1} (Supplementary Fig. S3a). Significantly, a 22 cm^{-1} shift of the Si–O stretching vibration from 1105 to 1083 cm^{-1} was observed in the presence of surface-attached Sb_2S_3 nanoparticles, indicating a change in the vibration environment of the Si–O bonds in the as-synthesized Sb_2S_3/HNTs, possibly due to the formation of covalent S–Sb bonds on the surface of the thiol-functionalized HNTs (Supplementary Fig. S3a). (The electronegativity difference between S (2.58) and Sb (2.05) is only 0.53, and the S–Sb bond length (2.40 Å) is greater than that of S–H (1.35 Å), implying a decrease in the vibration frequency). FTIR spectra of the calcined product confirmed complete loss of the polymer component, and showed no further change in the Si–O stretching frequency from the shifted value of 1083 cm^{-1}, implying that the S–Sb bonds remained intact after thermal treatment (Supplementary Fig. S3b).

XPS measurements were carried out to identify the surface chemical composition and the oxidation state for the as-synthesized Sb_2S_3/HNTs (Supplementary Fig. S4). In general, no obvious impurities were detected in the XPS survey spectrum (Supplementary Fig. S4a) of the as-synthesized Sb_2S_3/HNTs, which showed only a weak Si 2p

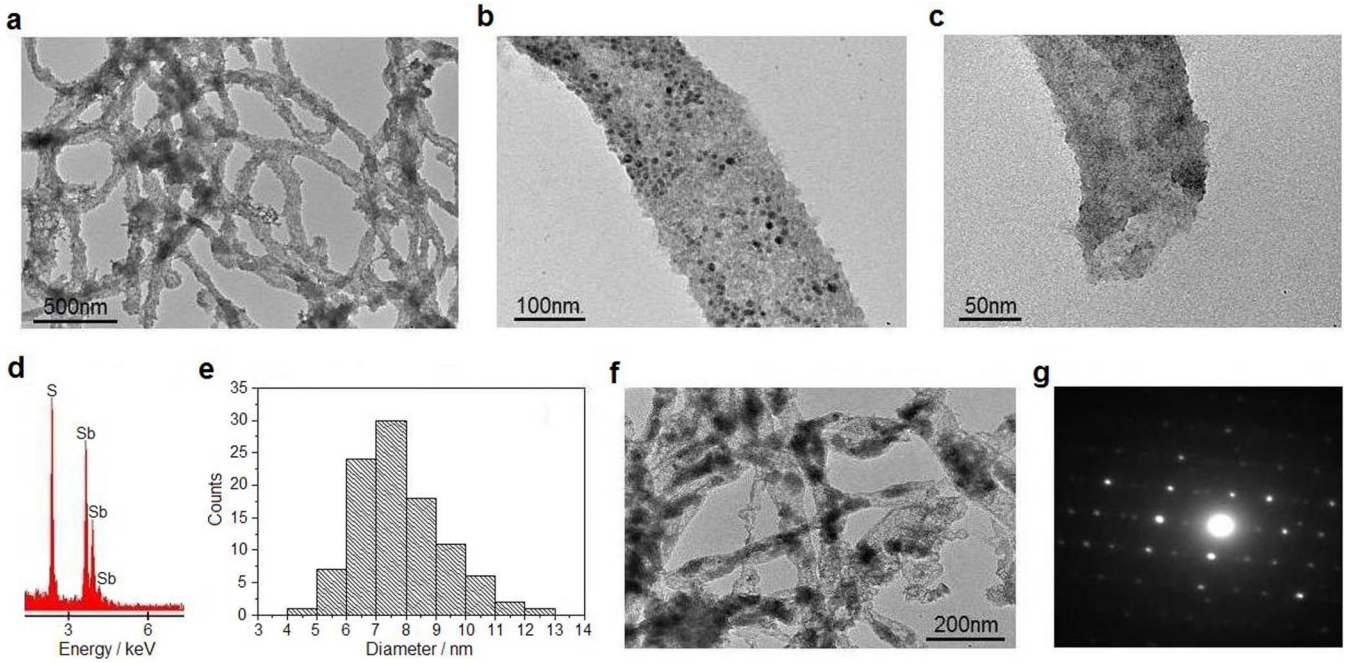

Figure 2 | Morphologies of as-synthesized and calcined Sb_2S_3/HNTs. (a) TEM images of as-synthesized Sb_2S_3/HNTs nanocomposites at low magnification. (b) Single HNT coated with uniform Sb_2S_3 nanoparticles embedded in the surface silica coating. (c) Open end of a single HNT with associated silica matrix and Sb_2S_3 nanoparticles viewed at high magnification. (d) Representative EDX spectrum. (e) Size distribution diagram of Sb_2S_3 nanoparticles shown in (b). (f) TEM image of calcined Sb_2S_3/HNTs at 400°C under N_2. (g) Corresponding SAED pattern.

peak due to the uniform coverage of Sb_2S_3 nanoparticles on the surface of the HNTs as observed by TEM (Fig. 2). Values for the Sb:S molar ratio of 1 : 1.51 and 1 : 1.70 were determined for a control sample of as-synthesized Sb_2S_3 and Sb_2S_3/HNTs, respectively, consistent with a stoichiometry of Sb_2S_3, with surplus sulfur in the latter arising from the HNTs template. The high-resolution XPS profiles of the main constituents (Sb 3d, S 2p, O 1s and C 1s) of the as-synthesized Sb_2S_3/HNTs nanocomposite surface showed peak positions for both Sb 4d and S 2p at around 33.65 and 162.10 eV, respectively[24], and the two observed orbital peaks for Sb $3d_{5/2}$ (529.42 eV) and Sb $3d_{3/2}$ (538.83 eV) (Supplementary Fig. S4b)[3,6], confirmed the presence of Sb(III). These values were very similar to those determined in the control sample of amorphous Sb_2S_3 (Sb 3d, 529.60 and 538.97 eV), implying that the binding energy of Sb 3d remained unchanged before and after assembly on the surface of the HNTs. The S 2p region of the XPS profile for the as-synthesized Sb_2S_3/HNTs was composed of three contributions (Supplementary Fig. S4c); two main peaks at binding energies of 162.16 and 161.10 eV that were attributed to a single doublet from S–Sb bonds, and a relatively low intensity peak at 163.2 eV from C–SH bonds of the HNTs[25]. The peak at 162.10 eV showed a local chemical shift compared with that of the control Sb_2S_3 sample (161.58 eV), consistent with the formation of S–Sb bonds between the thiolated residues of the HNT template and Sb(III) ions on the surface of the assembled Sb_2S_3 nanoparticles, as also suggested by FTIR analysis (Supplementary Fig. S3). The position of the O 1s binding energy was superposed with that of the S $3d_{5/2}$ binding energy (Supplementary Fig. S4b). However, a broader high-resolution XPS profile of the O 1s region showed O 1s peaks at 532.09 and 533.44 eV that were ascribed to contributions from C–O/C=O bonds and Si–O/adsorbed H_2O, respectively[26]. Observation of the small Si 2p peak at 103.05 eV (Supplementary Fig. S4a), corresponding to Si–O of SiO_2[27], further confirmed the presence of silica under the packed array of Sb_2S_3 nanoparticles. Deconvolution of the C 1s region showed two peaks at 284.79 and 286.24 eV, which were attributed respectively to the C–C and C–O (or C–SH) contributions of the as-synthesized Sb_2S_3/HNTs.

The optical properties of the as-synthesized and calcined Sb_2S_3/HNTs were investigated by solid-state UV-vis absorption spectroscopy, which showed absorbance peaks at around 460 or 670 nm, respectively, with the latter comprising an extended absorption edge of about 750 nm (Supplementary Fig. S5a). Direct band gap energies were determined by fitting the absorption data to the direct transition equation[28], which gave values of 2.10 and 1.67 eV for the amorphous (as-synthesized) and crystalline forms of Sb_2S_3 (calcined), respectively. The latter value was lower than that of other reports on crystalline Sb_2S_3 (1.78–2.50 eV)[29], suggesting that the Sb_2S_3/HNTs nanocomposite may have potential applications in solar energy and photoelectronic devices. The red-shift in the absorption edge and direct band gap decrease is directly associated with crystallization of the amorphous Sb_2S_3 phase[6]. The amorphous Sb_2S_3/HNTs can be considered as a degenerate direct band gap semiconductor due to the high density of defects and the existence of a large number of states within the energy gap. This was consistent with a plot of $(\alpha h\nu)^2$ *vs.* $h\nu$ (α is the optical absorption coefficient) for the amorphous as-synthesized sample (Supplementary Fig. S5b), which showed an exponential-like tailing of the straight line; that is, the absorption decreased slowly compared to the crystalline calcined Sb_2S_3 material below the optical gap. To determine the valence band (VB) and conduction band (CB) positions of the samples, we theoretically calculated the band edge positions of the materials using the atomic electronegativities of the constituent atoms[30,31]. The calculated E_{VB} of the calcined Sb_2S_3/HNTs was 1.97 eV, similar to that of pure Sb_2S_3 (E_{VB} = 1.98 eV), suggesting that it would also be an potential excellent visible-light responsive photocatalyst in the environmental fields. Laser confocal scanning microscopy was used to record the fluorescence spectra of different samples. As expected, the fluorescence intensities in the presence of Sb_2S_3 were much higher than the native HNTs with the as-synthesized Sb_2S_3/HNTs nanocomposites exhibiting higher fluorescence intensities than control samples

of amorphous Sb_2S_3 (Supplementary Fig. S6). Although morphological factors, quantum effects and coupling can influence the fluorescence intensity[32], the uniform distribution of Sb_2S_3 nanoparticles on the surface of the HNTs might be responsible for the higher intensity by allowing increased numbers of electron and holes to return to the ground state via optically radiative recombination routes.

We simulated a surface structure model of amorphous silica by using crystalline approximations (Supplementary Fig. S7)[33], and constructed the thiol-functionalized silica surface of the native HNTs by replacing the surface hydroxyl groups of amorphous silica with mercaptopropyl groups (Fig. 3a–c). Density functional theory (DFT) calculations gave an average Si–O bond length of 1.60 Å (Supplementary Fig. S8b). Whilst there were two distinct Si–O bonds with slightly different bond lengths in the bulk silica crystal, the Si–O bond lengths were all very close to 1.60 Å after full relaxation of the whole slab, consistent with the amorphous structure[34]. The average bond lengths of C–C, C–S and S–H in the covalently linked $-(CH_2)_3SH$ surface group were calculated to be 1.517, 1.812 and 1.356 Å (Supplementary Fig. S8d–f), respectively, which agreed well with previous experimental results (1.524, 1.808, 1.340 Å)[35,36]. Moreover, hydroxyl groups positioned at the base of the surface layer

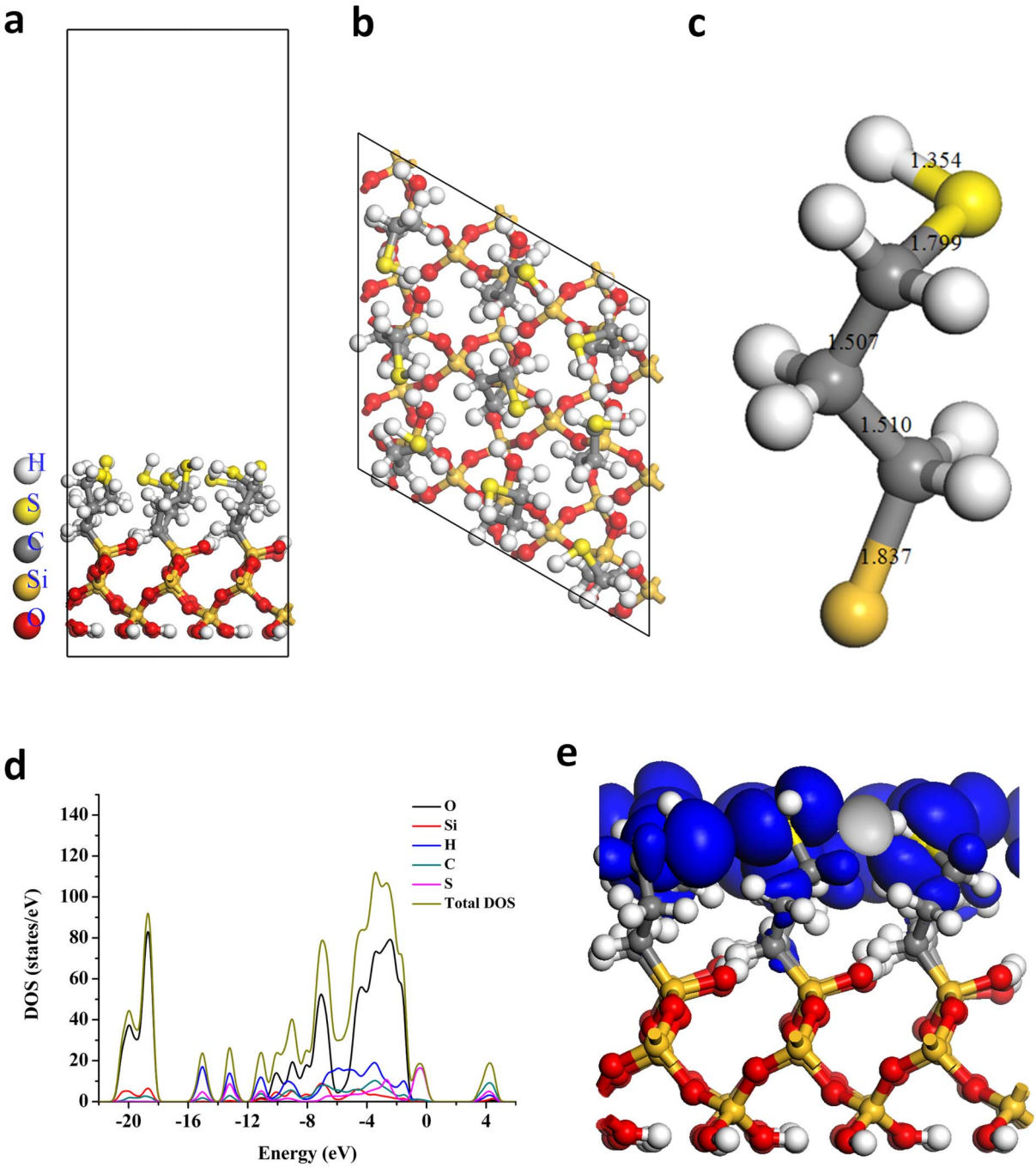

Figure 3 | Geometric structure and electronic properties of thiol-functionalized silica surface. (a) Side view and (b) top view showing mercaptopropyl groups. (c) Single Si–$(CH_2)_3SH$ chain showing bond distances in Å. (d) Total density of states (DOS) and atom-projected density of states (PDOS) for the silica surface of HNTs covalently functionalized with pendent mercaptopropyl groups. (e) Partial charge density of the HNT surface, corresponding to the band above the valence band maximum (VBM). The isosurface levels are 0.01 e/Å^3.

were in an approximately parallel conformation (Fig. 3a), facilitating the formation of surface hydrogen bonds between nearest neighboring hydroxyls. In contrast, the top of the mercaptopropyl-functionalized silica surface consisted of a diverse distribution of thiol groups due to the abundant lone pairs on the sulfur atoms. In order to gain deeper insight into the strong influence of the mercaptopropyl groups on the *in situ* surface environment, we performed a dynamic analysis of the HNTs surface structure. Significantly, the bond length distributions in the $-(CH_2)_3SH$ moiety after 5 ps dynamic equilibrium (Supplementary Fig. S9) demonstrated that the pendent $-C_3H_6SH$ group altered the SiNTs surface to a rather flexible and variable organic surface, showing a heterogeneous surface structure of covalently linked pendent mercaptopropyl groups.

The valence bands associated with the unfunctionalized silica surface consisted of O 2p states, while the conduction bands were formed from a mixture of O 2s, H 1s, and Si 3s states (Supplementary Fig. S7c). Calculation of the density of states (DOS) and partial charge density for the mercaptopropyl-functionalized silica surface of the HNTs indicated that the lower and upper valence bands were composed of mainly O 2s or O 2p, respectively, along with states hybridized with the $-(CH_2)_3SH$ group (Fig. 3d, e). The conduction band near the conduction band maximum (CBM) was mainly a H 1s state, partly hybridized with S 3p states. The most significant change associated with surface attachment of the mercaptpropyl groups was that the lone pair on the S atom introduced a localized band above the valance band maximum (VBM) of pure silica, which contained some states consisting of mixtures of S 3p with C 2p and H 1s states. This was clearly shown in the partial charge density of the HNTs surface (Fig. 3d). Interestingly, the band gap reduced to a value of 3.75 eV, indicating that the HNTs should show a much stronger UV light absorption and chemical reactivity than the pure silica surface.

Given the above FTIR spectroscopic and XPS investigations, we investigated the formation of S–Sb interfacial binding through molecular simulation methods. Previously, it has been reported that a fully hydrogenated silica surface was inert with respect to the adsorption of Au atoms, even though the binding energy between Au and Si surface dangling bonds (3.8 eV) or O dangling bonds (2.7 eV) was higher than that between Au and any surface site at the TiO_2 surface[37]. Since the bonding nature is still confusing[38], based on previous research on the adsorption of thiols on Au surfaces[39], we performed DFT calculations for the interfacial binding between Sb_2S_3 nanoparticles and the deprotonated HNTs surface. The DOS for the Sb_2S_3/HNTs nanocomposites surface structure remained the same as the algebraic sum of the DOS of Sb_2S_3 and that of the HNTs surface before and after physisorption. However, similar to bond formation between Au and –SH[40], chemisorption leads to covalent bond formation at the interface to produce a significant change in the electronic structure for the nanocomposites that resulted from electron-stimulated hydrogen desorption (The detailed DOS for the three samples are given in Supplementary Fig. S10). The DOS of the Sb_2S_3/HNTs nanocomposites near the Fermi energy was greatly affected by the formed S–Sb covalent bond (Fig. 4). It was observed that the band gap of the nanocomposites was dependent on the highest occupied molecular orbital/lowest unoccupied molecular orbital (HOMO–LUMO) gap of the assembled Sb_2S_3 nanoparticles in region I, indicating that the highest optical adsorption wavelength should not be obviously changed after chemisorption. However, the rather localized mixed states of Sb_2S_3 and the HNTs overlap in region II, and the mixed charge density in region III demonstrates that significant electronic structure changes occur upon the formation of S–Sb covalent bonds during the adsorption process.

Fig. 5 shows the calculated charge density difference at the Sb_2S_3/HNTs interface. Charge transfer was particularly noticeable at the Sb–S bond traversing the interface between Sb atoms of the Sb_2S_3 nanoparticle and S atoms of the thiol moiety on the HNTs surface (see dotted circles in Fig. 5b). The Mulliken charges on the Sb and S

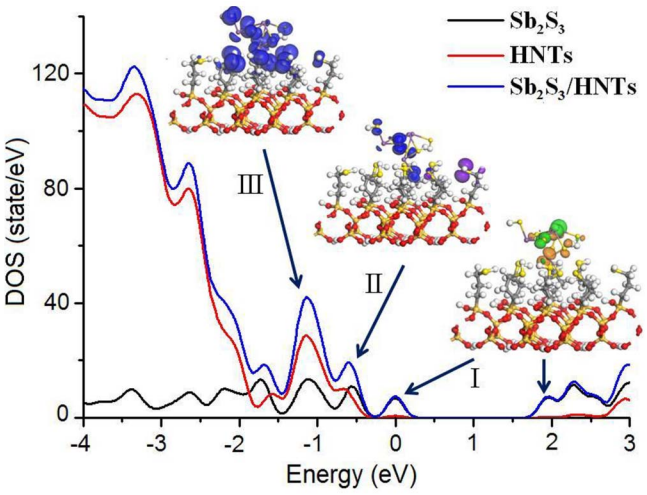

Figure 4 | Partial charge density corresponding to the near band gap states. The isosurface levels were 0.01 e/Å^3. The brown and green line in region I represent CBM and VBM states, the blue and purple line in region II represent valence band states near VBM, and the blue line in region III represent the lower valence band states.

atoms in the Sb_2S_3 nanoparticles ranged from 0.41 to 0.66 e, and −0.37 to −0.56 e, respectively, which as expected were considerably less than values for the bulk structures due to the decreased coordination numbers associated with atoms in nanoscale clusters or at surface sites. With regard to the HNTs template, the Mulliken charges of the S atoms ranged from −0.11 to −0.14 e, corresponding to the observed by XPS data that showed a higher binding energy (162.10 eV) of S 2p compared to that of the S atoms (161.58 eV) in Sb_2S_3. The charges of Sb, S, C at the relaxed nanocomposite interface were 0.93 e, −0.22 e, 0.61 e, respectively (Fig. 5b), which were different from the charges of 0.63 e, −0.15 e, 0.64 e before chemisorption, indicating significant charge transfer at the Sb_2S_3/HNTs interface. These theoretical calculations coincided well with the experimental results, revealing the origin of the interfacial affinity of the mercaptopropyl functional groups for the Sb_2S_3 nanoparticles and their strong aggregation onto the outer surface of the HNTs.

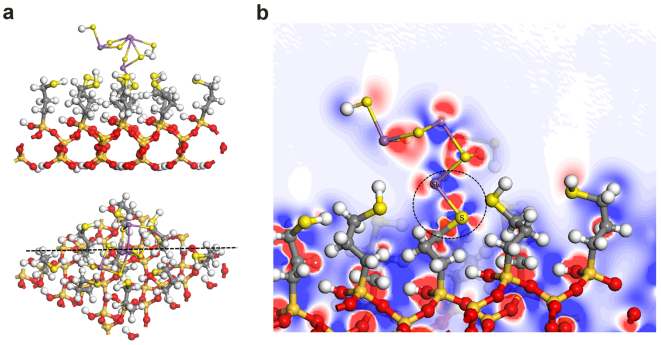

Figure 5 | Interface between Sb_2S_3 nanoparticles and HNTs. (a) Side (upper panel) and top (lower panel) view of the interface between Sb_2S_3 nanoparticles and the mercaptpropyl-functionalized silica surface of a HNT in Sb_2S_3/HNT nanocomposites. (b) Charge density difference of the Sb_2S_3/HNT interface plotted along the plane designated by the dotted lines shown in the lower panel of (a). Blue corresponds to charge depletion and red to charge gain. Isosurfaces are shown in the range [−0.05, 0.05] (e/Å3). Contours of constant charge density are separated by 0.003 eV/Å^3. The small yellow or violet balls represent S or Sb atoms, respectively, in Sb_2S_3 nanoparticles. The large yellow, black, or white balls represent S, C, or H atoms in the HNT surface.

Although a similar mode of charge transfer was determined for the interfaces between thiol groups and Au or Ag atoms[29,41–43], the details of the mechanism remains obscure. We hope our results therefore provide both specific and general insights into the nature of interfacial interactions in multi-component nanomaterials with integrated structure and function.

Discussion

As for the synthesis of Sb_2S_3/HNTs, we also investigated the influence of the Sb:Si molar ratio, as well as the effect of the order of addition of the reactants, on the fidelity of the templating process. No significant modifications in the as-synthesized or calcined materials were observed when the Sb:Si molar ratio was changed from 1 : 1 to 1 : 10, which corresponded to Sb_2S_3: silica mass ratios ranging from 17 : 6 to 17 : 60, respectively, in the hybrid materials. However, at Sb:Si = 1 : 10, the relatively low Sb content resulted in sporadic deposition of Sb_2S_3 nanoparticles across the surface of the silicified polymer tubules rather than a uniform distribution (Supplementary Fig. S11a, b and S12). Under these conditions, the reduced rate of inorganic nucleation was also associated with an approximate two-fold increase in the mean size of the individual Sb_2S_3 nanoparticles to a value of 15.6 nm. Interestingly, replacing the simultaneous addition of TAA and HNTs to the antinomy chloride solution with a procedure in which TAA was added first, followed by an aliquot of the HNTs suspension only after the reaction solution had turned orange in color, also produced silicified polymer myelin tubules coated with uniform-sized Sb_2S_3 nanoparticles, 11.0 nm in mean size (Supplementary Fig. S11c). Although we could not rule out the possibility of primary nucleation occurring directly on the surface of the nanotubular template, our results suggested that formation of Sb_2S_3 nanoparticles in solution followed by strong adsorption onto the surface of the thiol-functionalized silica-coated polymer nanotubes was the principal mechanism underlying the surface decoration process. Our results also indicate that non-equilibrium processes of $E_{16}B_{22}$ myelination can be used to prepare thiol-functionalized, polymer/silica HNTs with high shape anisotropy, which in turn can be exploited as nanostructured templates for the controlled spatial deposition of amorphous Sb_2S_3 and its subsequent transformation to silica fibres embedded with crystalline Sb_2S_3 nanoparticles.

In summary, the uniform Sb_2S_3 nanoparticles were spontaneously assembled as packed arrays on thiol-functionalized silica/polymer myelin-like nanotubular templates to produce novel hybrid multifunctional nanocomposites. A theoretical prototype of a hybrid Sb_2S_3/silica nanotube surface structure was proposed, and DFT calculations of the geometric structure and the electronic properties provided a deeper insight into the role played by the mercaptopropyl groups in the attachment of nanoparticles to the silicified outer locating of the HNT substrate. The major optical property of the prepared hybrid nanocomposites was determined by the electron states of the assembled Sb_2S_3 nanoparticles, while the electronic property of each component was considerably hybridized. Charge transfer from Sb_2S_3 to the HNTs substrate was confirmed. Our approach may pave a way towards the engineering of hybrid nanostructures as versatile platforms for the synthesis and assembly of nanoparticles to produce nanocomposites with tailored and enhanced functional properties. Moreover, the electronic structure information derived from DFT calculations reported herein could benefit the future atomic-level analysis of hybrid nanocomposites in general.

Methods

Materials synthesis. Hybrid nanotubes of thiol-functionalized silica–$E_{16}B_{22}$ myelin nanotubes (HNTs) were synthesized according to our previous work[21]. Typically, poly (ethylene oxide)-b-poly (1,2-butylene oxide) ($E_{16}B_{22}$, M_n = 2300, PI: 1.13, APM, Canada) was mixed with tetraethoxysilane (TEOS) and 3-mercaptopropyl triethoxysilane (MTEOS) [$HS(CH_2)_3Si(OC_2H_5)_3$] at a molar ratios of $E_{16}B_{22}$:TEOS:MTEOS = 1 : 3.5 : 3.5. Aqueous NH_4OH (125 mM, pH 10.8) was added to the mixture to give a final concentration of 0.1 wt% of $E_{16}B_{22}$ in water. The resulting dispersion was sonicated in a water bath for 1 min and then left unstirred at 22–25°C for 3 days to produce thiol-functionalized silica/polymer myelin-like nanostructures. The preparation of Sb_2S_3/HNTs nanocomposites was performed via a novel room-temperature procedure. Typically, 0.0571 g antimony chloride ($SbCl_3$, 99.99%, Aldrich) was dissolved in 5 mL ethylene glycol (EG, 99%, Aldrich) in a capped glass bottle to form a colorless solution. 0.0376 g of thioacetamide (TAA, 99%, Sigma-Aldrich), along with a suspension of pre-prepared HNTs were simultaneously added to the clear solution at a Sb:Si molar ratio from 1 : 1 to 1 : 10. After stirring for 1 min, the solution became lemon-yellow in color, followed by the formation of an orange precipitate after 5 min. Leaving the suspensions unstirred for 24 h at room temperature resulted in a brick-red precipitate, which was separated by centrifugation, washed with anhydrous ethanol several times, and then vacuum-dried at 70°C for 10 h in air to produce the as-synthesized Sb_2S_3/HNTs samples. Thermal treatment of the as-synthesized materials was carried out at 400°C for 6 h under N_2 (flowing rate of 1 L/min) with a heating rate of 2°C/min in a tube furnace. Pure Sb_2S_3 was synthesized according to the same experimental process without addition of a dispersion of HNTs.

Characterization. X-ray diffraction (XRD) measurements were carried out using a Bruker Advance powder diffractometer with Cu Kα radiation (λ = 0.15406 nm). A transmission electron microscope (TEM, JEOL JEM-1200EX, 120 kV) was used for morphological analysis of the samples. High-resolution transmission electron microscope (HRTEM) images and selected area electron diffraction (SAED) patterns were recorded on a JEOL JSM 3010 electron microscope operating at 200 kV. Energy dispersive X-ray (EDX) analysis of the samples was carried out on an OXFORD instrument attached to the HRTEM instrument in the scanning range of 0–30 eV. Fourier transform infrared spectroscopy (FTIR) spectra of the samples were collected on a PERKIN ELMER Spectrum One FTIR spectrometer using KBr discs in the range of 4000–400 cm^{-1}. Thermogravimetric differential scanning calorimetry (TG–DSC) was performed in air using a Netzsch STA 409EP simultaneous thermal analyzer at a heating rate of 5°C/min. X-ray photoelectron spectroscopy (XPS) analysis was performed on a Thermo ESCALAB 250 spectrometer equipped with an Al $K\alpha$ (1486.6 eV) monochromator X-ray source. The spectra were calibrated by using the adventitious carbon C1s (284.6 eV) peak. High-resolution XPS data were fitted with Gaussian–Lorentz functions after background subtraction using the ESCALAB v1.5 data processing software under the constraint of setting a reasonable binding energy (BE) shift and full width at half-maximum range (FWHM). Liquid phase ultraviolet-visible (UV-vis) diffuse reflectance spectra were measured using a Perkin-Elmer Lambda 25 UV-vis spectrometer at room temperature. A Shimadzu UV-2550 UV-visible spectrophotometer was used to obtain the absorption spectra of the solid samples with a wavelength range of 200–800 nm using $BaSO_4$ as a reference material. The band gap energy was determined by fitting the absorption data to the direct transition equation; $(\alpha h\nu)^2 = A(h\nu - E_g)$, where α is the optical absorption coefficient, $h\nu$ is the corresponding phonon energy, E_g is the direct band gap energy, and A is a constant. Plotting $(\alpha h\nu)^2$ as a function of $h\nu$, and extrapolating the linear portion of the spectra to $\alpha h\nu = 0$, gave the values of the direct band gap (E_g). The valence band (VB) position was estimated by the following empirical equation: $E_{VB} = X - E^e + 0.5E_g$, where E_{VB} is the VB edge potential, X the electronegativity of the sample, which is the geometric mean of the electronegativity of the constituent atoms (5.63 eV for Sb_2S_3), E^e is the energy of free electrons on the hydrogen scale (≈4.5 eV), and E_g is the band gap energy of the sample. A Leica TCS-SP2-AOBS laser confocal scanning microscope (attached to a Leica DM IRE2 inverted epiflurescence microscope) was employed to analyze the fluorescence intensity of the samples. Raman spectra were acquired with a Renishaw RCH22 spectrometer, using a laser excitation wavelength of 514 nm (green). The samples were placed onto a glass microscope slide, and the laser focused onto the top surface to maximize the signal. Spectra were recorded between 100–1000 cm^{-1}.

Calculations. All calculations were performed with the program CASTEP (Cambridge Sequential Total Energy Package) code, based on first–principle density functional theory (DFT). Both the local density approximation (LDA) and generalized gradient approximation (GGA) with the exchange-correlation potential by Perdew, Burke and Ernzerhof (PBE), were used for the calculations[44]. The ultrasoft pseudo-potential plane-wave formalism was applied for efficient computation. An energy cutoff of 400 eV was used. The Monkhorst-Pack grid with sufficiently dense k points mesh was used for the convergence of the results and accurate calculation of the density of electronic states, whilst Gamma point was used for geometrical calculations. The self-consistent total energy in the ground state was effectively obtained by the density-mixing scheme. During the geometry optimizations, the convergence threshold for self-consistent field (SCF) tolerance was set to 1.0×10^{-6} eV/atom, all forces on the atoms were converged to less than 0.03 eV/Å, the total stress tensor was reduced to the order of 0.05 GPa, and the maximum ionic displacement was within 0.001 Å. The cell parameters and atomic coordination of bulk Sb_2S_3 and silica structures were optimized during the geometry optimization using a Broyden-Fletcher-Goldfarb-Shanno (BFGS) minimization algorithm[45]. Two schemes were tested for the silica surface structure. As similar electronic structure results have been obtained for the two surface structures cleaved from both the native bulk structures and the relaxed bulk structures, we adopted the original cell parameters for the following calculations. The slab thickness of silica was varied from 5.2 Å to 14.1 Å, corresponding to three to six layers, and no change in the electronic structure of silica was determined. Thus, a three-layer thick slab was considered in

this work. Furthermore, in order to avoid the fictitious interaction between the assembled Sb_2S_3 nanoparticles resulting from the periodic boundary condition, the 3×3 extended periodic silica (001) surface of 14.739×14.739 Å was adopted. Furthermore, we employed a HNT model surface structure with the surface –OH groups replaced by $-(CH_2)_3SH$ moieties, giving a total of 216 atoms. The slabs were separated by a vacuum region of 25 Å along the perpendicular direction. The geometric and electronic properties were analyzed using both hydrated and dehydrated models before further investigations of the interface mechanism operating between the assembled nanoparticles and the HNTs substrate. The interfacial model comprising suitable structures was then considered an appropriate theoretical description to elucidate the experimental observations.

1. Parise, J. B. An antimony sulfide with a two-dimensional, intersecting system of channels. *Science* **251**, 293–294 (1991).
2. Juárez, B. H., Rubio, S., Sánchez-Dehesa, J. & López, C. Antimony Trisulfide Inverted Opals: Growth, Characterization, and Photonic Properties. *Adv. Mater.* **14**, 1486–1490 (2002).
3. Yang, R. B. *et al.* Pulsed Vapor-Liquid-Solid Growth of Antimony Selenide and Antimony Sulfide Nanowires. *Adv. Mater.* **21**, 3170–3174 (2009).
4. Baghbanzadeh, M., Carbone, L., Cozzoli, P. D. & Kappe, C. O. Microwave-assisted synthesis of colloidal inorganic nanocrystals. *Angew. Chem. Int. Edit.* **50**, 11312–11359 (2011).
5. Lim, C.-S. *et al.* Hole-conducting mediator for stable Sb_2S_3-sensitized photoelectrochemical solar cells. *J. Mater. Chem.* **22**, 1107–1111 (2012).
6. Salinas-Estevané, P. & Sánchez, E. M. Preparation of Sb_2S_3 Nanostructures by the Ionic Liquid-Assisted Sonochemical Method. *Cryst. Growth Des.* **10**, 3917–3924 (2010).
7. Castro, J. R. *et al.* Formation of antimony sulfide powders and thin films from single-source antimony precursors. *J. Mater. Chem.* **18**, 5399–5405 (2008).
8. Lou, W., Chen, M., Wang, X. & Liu, W. Novel single-source precursors approach to prepare highly Uniform Bi_2S_3 and Sb_2S_3 nanorods via a solvothermal treatment. *Chem. Mater.* **19**, 872–878 (2007).
9. Ota, J. & Srivastava, S. K. Tartaric acid assisted growth of Sb_2S_3 nanorods by a simple wet chemical method. *Cryst. Growth Des.* **7**, 343–347 (2007).
10. Mann, S. Self-assembly and transformation of hybrid nano-objects and nanostructures under equilibrium and non-equilibrium conditions. *Nat. Mater.* **8**, 781–792 (2009).
11. Hoffmann, F., Cornelius, M., Morell, J. & Fröba, M. Silica-based mesoporous organic-inorganic hybrid materials. *Angew. Chem. Int. Edit.* **45**, 3216–3251 (2006).
12. Vallé, K., Belleville, P., Pereira, F. & Sanchez, C. Hierarchically structured transparent hybrid membranes by in situ growth of mesostructured organosilica in host polymer. *Nat. Mater.* **5**, 107–111 (2006).
13. Soler-Illia, G. J. A. A. & Azzaroni, O. Multifunctional hybrids by combining ordered mesoporous materials and macromolecular building blocks. *Chem. Soc. Rev.* **40**, 1107–1150 (2011).
14. Stein, A., Melde, B. J. & Schroden, R. C. Hybrid inorganic-organic mesoporous silicates-nanoscopic reactors coming of age. *Adv. Mater.* **12**, 1403–1419 (2000).
15. Ruiz-Hitzky, E., Aranda, P., Darder, M. & Ogawa, M. Hybrid and biohybrid silicate based materials: molecular vs. block-assembling bottom-up processes. *Chem. Soc. Rev.* **40**, 801–828 (2011).
16. Chamberlain, T. W. *et al.* Reactions of the inner surface of carbon nanotubes and nanoprotrusion processes imaged at the atomic scale. *Nat. Chem.* **3**, 732–737 (2011).
17. Pack, S. *et al.* Segregation of carbon nanotubes/organoclays rendering polymer blends self-extinguishing. *Macromolecules* **42**, 6698–6709 (2009).
18. Zanolli, Z. *et al.* Gas sensing with Au-decorated carbon nanotubes. *ACS Nano* **5**, 4592–4599 (2011).
19. Ben-Ishai, M. & Patolsky, F. Wall-selective chemical alteration of silicon nanotube molecular carriers. *J. Am. Chem. Soc.* **133**, 1545–1552 (2011).
20. Park, M.-H. *et al.* Silicon nanotube battery anodes. *Nano Lett.* **9**, 3844–3847 (2009).
21. Li, M. & Mann, S. Emergent hybrid nanostructures based on non-equilibrium block copolymer self-assembly. *Angew. Chem. Int. Edit.* **47**, 9476–9479 (2008).
22. Sanchez, C., Julián, B., Belleville, P. & Popall, M. Applications of hybrid organic–inorganic nanocomposites. *J. Mater. Chem.* **15**, 3559–3592 (2005).
23. Han, Q., Lu, J., Yang, X., Lu, L. & Wang, X. A Template-free route to Sb_2S_3 crystals with hollow olivary architectures. *Cryst. Growth Des.* **8**, 395–398 (2008).
24. Espinós, J. P. *et al.* ^{121}Sb Mössbauer and X-ray photoelectron spectroscopy studies of the electronic structure of some antimony misfit layer compounds. *Chem. Mater.* **9**, 1393–1398 (1997).
25. Kankate, L., Turchanin, A. & Gölzhäuser, A. On the release of hydrogen from the S-H groups in the formation of self-assembled monolayers of thiols. *Langmuir* **25**, 10435–10438 (2009).
26. Yang, H. & Tao, Q. Sol-gel Synthesis and characterization of CeO_x-SiO_2-TiO_2 thin films. *J. Am. Ceram. Soc.* **93**, 1056–1061 (2010).
27. Reddy, B. M. *et al.* Surface characterization of CeO_2/SiO_2 and $V_2O_5/CeO_2/SiO_2$ catalysts by Raman, XPS, and other techniques. *J. Phys. Chem. B* **106**, 10964–10972 (2002).
28. Maensiri, S., Masingboon, C., Promarak, V. & Seraphin, S. Synthesis and optical properties of nanocrystalline V-doped ZnO powders. *Opt. Mater.* **29**, 1700–1705 (2007).
29. Savadogo, O. & Mandal, K. C. Studies on new chemically deposited photoconducting antimony trisulphide thin films. *Sol. Energ. Mat. Sol. Cell.* **26**, 117–136 (1992).
30. Kim, Y. I., Atherton, S. J., Brigham, E. S. & Mallouk, T. E. Sensitized layered metal oxide semiconductor particles for photochemical hydrogen evolution from nonsacrificial electron donors. *J. Phys. Chem.* **97**, 11802–11810 (1993).
31. Lin, X. *et al.* Photocatalytic activities of heterojunction semiconductors Bi_2O_3/$BaTiO_3$: A strategy for the design of efficient combined photocatalysts. *J. Phys. Chem. C* **111**, 18288–18293 (2007).
32. Wan, J., Wang, Z., Chen, X., Mu, L. & Qian, Y. Shape-tailored photoluminescent intensity of red phosphor Y_2O_3:Eu^{3+}. *J. Cryst. Growth* **284**, 538–543 (2005).
33. Hossain, M. Z. Chemistry at the graphene-SiO_2 interface. *Appl. Phys. Lett.* **95**, 143125–143127 (2009).
34. Orlandini, S., Ippolito, M. & Colombo, L. Mechanisms of self-diffusion in stoichiometric and substoichiometric amorphous silicon dioxide. *Phys. Rev. B* **81**, 1–8 (2010).
35. Nicovich, J. M., Kreutter, K. D., Van Dijk, C. A. & Wine, P. H. Temperature-dependent kinetics studies of the reactions $Br(^2P_{3/2}) + H_2S \leftrightarrow SH + HBr$ and $Br(^2P_{3/2}) + CH_3SH \leftrightarrow CH_3S + HBr$. Heats of formation of SH and and CH_3S radicals. *J. Phys. Chem.* **96**, 2518–2528 (1992).
36. Lide, D. R. CRC Handbook of Chemistry and Physics, 90th Edition (CRC Press, 2009).
37. Veith, G. M. *et al.* Thermal stability and catalytic activity of gold nanoparticles supported on silica. *J. Catal.* **262**, 92–101 (2009).
38. Rzepa, H. S. The importance of being bonded. *Nat. Chem.* **1**, 510–512 (2009).
39. Vericat, C., Vela, M. E., Benitez, G., Carro, P. & Salvarezza, R. C. Self-assembled monolayers of thiols and dithiols on gold: new challenges for a well-known system. *Chem. Soc. Rev.* **39**, 1805–1834 (2010).
40. Tielens, F. & Santos, E. AuS and SH bond formation/breaking during the formation of alkanethiol SAMs on Au(111): A theoretical study. *J. Phys. Chem. C* **114**, 9444–9452 (2010).
41. Castner, D. G., Hinds, K. & Grainger, D. W. X-ray photoelectron spectroscopy sulfur 2p study of organic thiol and disulfide binding interactions with gold surfaces. *Langmuir* **12**, 5083–5086 (1996).
42. Lam, K. F., Yeung, K. L. & McKay, G. A rational approach in the design of selective mesoporous adsorbents. *Langmuir* **22**, 9632–9641 (2006).
43. Nuzzo, R. G., Zegarski, B. R. & Dubois, L. H. Fundamental studies of the chemisorption of organosulfur compounds on gold (111). Implications for molecular self-assembly on gold surfaces. *J. Am. Chem. Soc.* **109**, 733–740 (1987).
44. Perdew, J. P., Burke, K. & Ernzerhof, M. Generalized gradient approximation made simple. *Phys. Rev. Lett.* **77**, 3865–3868 (1996).
45. Pfrommer, B. G., Côté, M., Louie, S. G. & Cohen, M. L. Relaxation of crystals with the quasi–newton method. *J. Comput. Phys.* **131**, 233–240 (1997).

Acknowledgements

This work was financially supported by the EPSRC (UK), the National Science Fund for Distinguished Young Scholars (51225403) and the Specialized Research Fund for the Doctoral Program of Higher Education (20120162110079).

Author contributions

S.M. conceived the project and wrote the final paper. H.M.Y. wrote initial drafts of the work. H.M.Y. and M.L. designed the experiments. H.M.Y. synthesized and characterized the materials. M.L. performed the synthesis of the hybrid silica/polymer nanotubes. A.D.T. analyzed the solid-state UV-vis and XPS spectra. H.M.Y. and L.J.F. carried out the first-principle calculations. All authors discussed the results and commented on the manuscript.

Additional information

Supplementary information accompanies this paper at http://www.nature.com/scientificreports

Competing financial interests: The authors declare no competing financial interests.

How to cite this article: Yang, H.M., Li, M., Fu, L.J., Tang, A.D. & Mann, S. Controlled Assembly of Sb_2S_3 Nanoparticles on Silica/Polymer Nanotubes: Insights into the Nature of Hybrid Interfaces. *Sci. Rep.* **3**, 1336; DOI:10.1038/srep01336 (2013).